INVESTIGATION OF NON-LINEAR STRUCTURAL DYNAMICS AND AEROELASTIC PROPERTIES OF STRUT-BRACED WINGS IN A CONCEPTUAL DESIGN STAGE

Demian J. Colombo-Acquarone[1] and Wolf R. Krüger[1]

[1]Deutsches Zentrum für Luft- und Raumfahrt
Bunsenstr. 10, 37073 Göttingen
d.colombo-acquarone@proton.me
wolf.krueger@dlr.de

Keywords: Strut-braced wing, geometric nonlinearity, conceptual design, aeroelasticity

Abstract: The strut is an additional load carrying element that alleviates the bending moment on the wing. It allows for the integration of higher aspect ratio wings, which produce less induced drag and thus reduce fuel consumption for a given mission. The Strut-Braced Wing (SBW) concept is investigated in the framework of the European Clean Aviation joint undertaking with the AWATAR (Advanced Wing mATuration And integRation) project [1]. In the first part of this work, the AWATAR SBW configuration is modeled in a Conceptual Load Analysis (CLA) tool to conduct parametric studies in search of a minimum structural mass configuration. The inclusion of the aileron efficiency constraint shifts the optimal strut attachment position from the front spar to the rear spar. The optimal configurations are exported as low fidelity beam models. The second part of this work presents the aeroelastic analysis performed in MSC Nastran for the derived beam models for two representative maneuver load cases. The inclusion of geometric non-linearity results in larger bending loads for structural components subject to a compressive load. Additionally, large in-plane bending loads in the wing result from the strut reaction. All optimal AWATAR configurations show flutter instability within the flight envelope. The inclusion of non-linear pre-stress in the flutter equation may stabilize the system or change the flutter speed and the critical flutter mode depending on the load case. The flutter mechanism is unaffected by the pre-stress.

1 INTRODUCTION

It is estimated that aviation causes 1-2% of the global CO_2 emissions [2]. Considering the present growth in aviation traffic of approximately 3-4% each year [3], this corresponds to a doubling effect of the emissions roughly every 20 years and represents a problem that must be tackled by the aviation industry. A prominent concept to improve aircraft efficiency and mitigate emission is the adoption of increased Aspect Ratio (AR) wings [4]. The induced drag is inversely proportional to the AR

$$C_{D,i} = \frac{C_L^2}{\pi e \mathrm{AR}}, \tag{1}$$

where $C_{D,i}$ is the induced drag coefficient, C_L is the lift coefficient, and e is the Oswald efficiency factor. Since the induced drag typically accounts for 25% of the total drag during cruise (and even up to 50% at lower speed conditions), the aerodynamic efficiency can be increased significantly. The Strut-Braced Wing (SBW) is one promising way to implement High Aspect Ratio Wings (HARW) on transport aircraft, thus reducing fuel burn and greenhouse gas emissions.

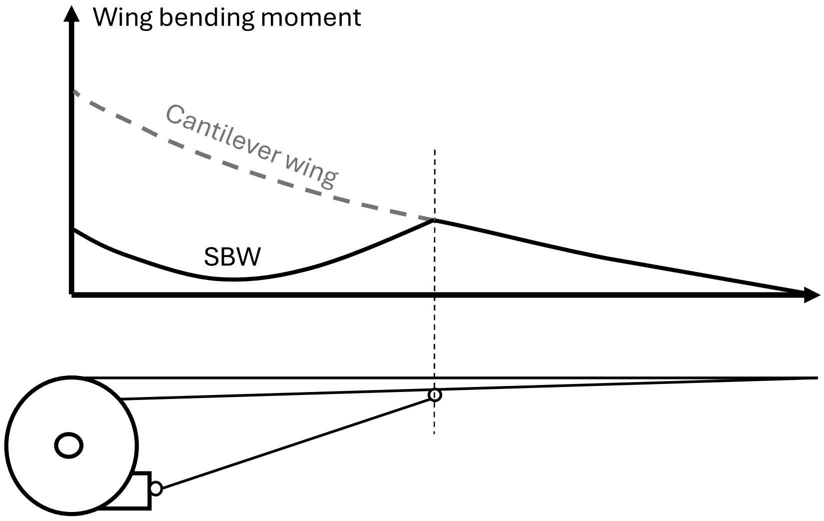

Figure 1: Qualitative bending moment comparison for a cantilever and strut-braced wing [5].

The strut is a support structure usually modeled as a rod or beam element, connected to the wing and the lower fuselage. The idea behind the braced wing concept is to reduce the bending loads on the wing, thus allowing for larger AR configurations. The strut is attached to the wing box somewhere between the front spar and the rear spar at an optimal spanwise position. A spherical, pinned or fixed attachment is possible. At the inboard end, the strut is attached either to the main landing gear sponson or any other structural component capable of carrying its loads and maximizing load sharing. For a conventional SBW configuration, the wing has a fixed connection to the fuselage and the strut has pinned connections on both sides, leading to a statically overdetermined system. The general SBW configuration and the qualitative bending load alleviation on the wing are shown in Fig. 1.

For a given load case, compressive or tensile loads develop in the wing due to the strut reaction force in the over constrained system. Additionally, large deformations of the HARW are expected. These combined effects may lead to substantial static non-linear geometry effects in the structural response [6], which may result in a considerable alteration of the eigenbehaviour of the SBW system. Subsequently, the flutter boundary becomes load case dependent, as has been thoroughly discussed in [7, 8]. Indeed, the variation in stiffness (differential stiffness) of the system has been found to influence eigenmode shapes and frequencies, as well as buckling instability in previous studies [9–11]. Hence, the classical approach of determining the flutter speed based on the mode shapes determined by a modal analysis of the unloaded structure may prove insufficient for SBW configurations. In which case, the non-linear behavior of the structure must be considered during the aeroelastic design. One approach is to integrate it into Multidisciplinary Design Optimization (MDO) studies to develop a general understanding of the investigated system at early development stages and fully exploit the synergistic potential of the SBW configuration. This approach has been implemented in [12] and is associated with a significant increase in computational cost compared to conventional MDO routines with a single run requiring up to 24 hours on a 60 core server.

Advanced Wing mATurAtion and integRation (AWATAR) is part of the larger Clean Aviation [13] joint undertaking co-funded by the European Union. The scope of AWATAR is to mature the design of an advanced wing with high fidelity simulations, wind tunnel tests and the development of a ground based demonstrator. The SBW concept is implemented to achieve

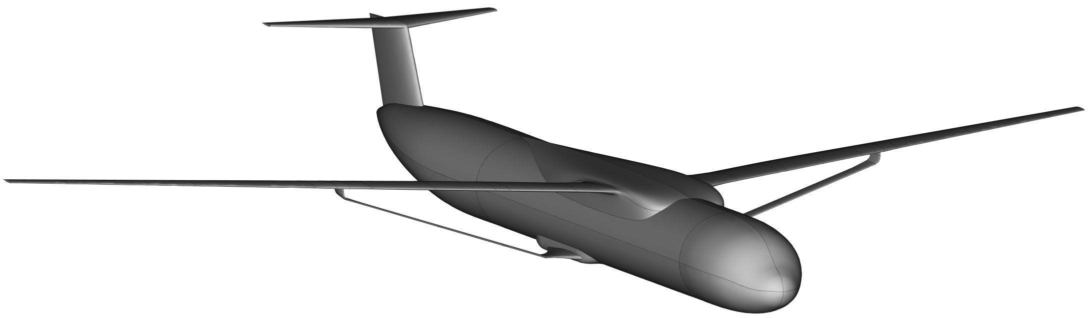

Figure 2: AWATAR baseline configuration.

an HARW with laminar flow characteristics on the outer wing area for a Short and Medium Range (SMR) aircraft. To assess the efficiency improvements of this concept, an Overall Aircraft Design (OAD) sizing loop is conducted, which also integrates an innovative propulsion system consisting of directly burned liquid hydrogen with an open fan engine. The twin-engine AWATAR aircraft depicted in Fig. 2 has an AR of 25, a maximum range of 2000 NM and can accommodate 200 passengers. The cruise altitude is 35000 ft and the cruise Mach number 0.78. Onera carried out the OAD and provided the aircraft specifications.

The goal of the present work is to develop a first understanding of the role of geometric non-linear effects on the static and dynamic aeroelastic response of the SBW configuration. First, a theoretical introduction to non-linear elastic beam theory and its application in Finite Elements Methods (FEM) is given in Sect. 2. An investigation of the SBW design of the AWATAR aircraft with the in-house Conceptual Load Analysis (CLA) tool follows in Sect. 3. The results from parametric studies conducted in [14] to find optimal configurations with minimum structural mass of the wing and strut are presented. The parametric variation includes the non-dimensional strut attachment position on the wing span η_{st} and chord ξ_{st}, the strut sweep angle Λ_{st}, the non-dimensional chordwise engine position ξ_{eng}, and the design cruise lift distribution shape factor N_{bell}. The role of aileron efficiency as an aeroelastic constraint in the parametric studies is discussed and the optimized configurations are exported as simple beam models. The aeroelastic analysis in MSC Nastran considering the effect of geometric non-linearity on the load distribution and the flutter response follows in Sect. 4. Sect. 5 concludes this work by providing a comprehensive summary of the results and highlighting future research possibilities.

2 GEOMETRIC NON-LINEAR BEAM BENDING

The elastic behavior of an aircraft wing is described by a set of three-dimensional partial differential equations. However, due to the complexity of the wing's structure, an exact analytical calculation is possible only in few (simple) cases. It is therefore common engineering practice to approximate complex structures with simplified mathematical models. Elastic beams are such classical elements that provide a good trade-off between model complexity and result accuracy. Indeed, HARW are frequently idealized as beams [15]. They allow for linear and non-linear formulations and are widely accessible in finite element software programs like MSC Nastran, ANSYS Mechanical, Abaqus, etc.

The elastic beam theory provides formulas to calculate internal loads, stresses and deformations from applied loads using partial differential equations and system specific boundary conditions. The classical Euler-Bernoulli beam theory assumes linear-elastic material properties with small and shear free deformations (shear modulus $G \to \infty$), effectively neglecting transverse deformations. In the case of geometric non-linear deformations, the equilibrium conditions must be formulated for the deformed system [16]. Geometric non-linear effects must be considered when the additional bending load from the equilibrium analysis for the deformed beam is significant compared to the linear bending load [6]. This is usually the case for systems with large axial loads and small deformations, systems with large deformations, and of course systems with both large axial loads and deformations. These conditions apply to the SBW aircraft configuration, where the strut's tensile or compressive force may induce large normal forces in the inboard wing while large deflections of the outboard wing are expected due to the high aspect ratio and slender structure.

The assumptions made in this section follow the Euler-Bernoulli beam theory [17]. The beam length is defined as l and the cross-section height and width as h and w respectively. The assumptions are summarized in the following:

- The beam axis in the unloaded state is straight or has a small curvature.
- The beam is slender ($l \gg h, w$).
- The beam elastic axis and the centroidal axis are equivalent.
- The material is linear-elastic, isotropic, and homogeneous in the beam cross-sections $A(x)$.
- Cross-sections don't experience warping, i.e. they remain planar after deformation (Bernoulli's first hypothesis).
- Cross-sections perpendicular to the beam axis remain perpendicular after deformation (Bernoulli's second hypothesis).

The relationship between stress σ and strain ε for idealized linear-elastic material deformation is given by Hook's law

$$\sigma = E\varepsilon \tag{2}$$

where E is Young's modulus.

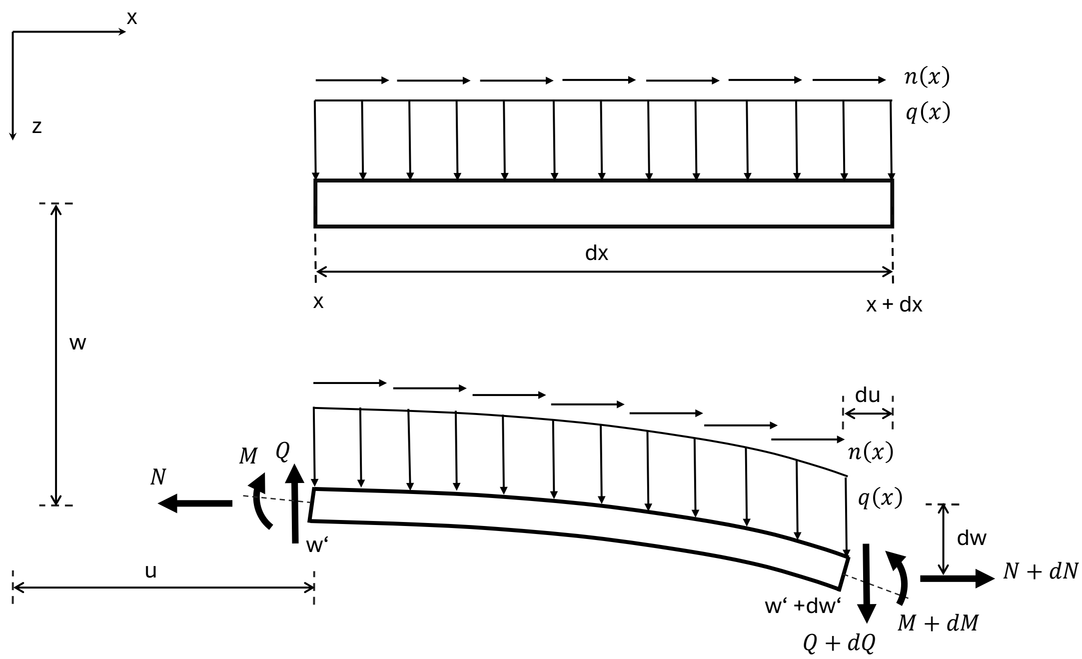

Figure 3: Equilibrium for the deformed beam element.

The forces and moments acting on the deformed beam are shown in Fig. 3. The equilibrium condition in x and z direction as well as around the y axis yields

$$\begin{aligned}
\sum F_x = 0 : dN + n(x)\, dx = 0 \quad &\Leftrightarrow \frac{dN}{dx} = N' = -n(x) \\
\sum F_z = 0 : dQ + q(x)\, dx = 0 \quad &\Leftrightarrow \frac{dQ}{dx} = Q' = -q(x) \\
\sum M = 0 : dM + N\, dw - Q\, dx = 0 \quad &\Leftrightarrow \frac{dM}{dx} + N\frac{dw}{dx} = Q.
\end{aligned} \tag{3}$$

The third term in Eq. 3 shows the influence of the normal force on the bending moment. Inserting the terms for N' and Q' into the term for M' yields the partial differential equation

$$\frac{d^2M(x)}{dx^2} + N\frac{d^2w(x)}{dx^2} - n(x)\frac{dw(x)}{dx} = -q(x). \tag{4}$$

The horizontal displacement $u(x, z)$ of any point on the beam under the assumption of moderate rotations and small strains is given by the kinematic relation

$$u(x, z) \approx u(x) - \frac{dw(x)}{dx}z. \tag{5}$$

The Green-Lagrange strain tensor

$$\varepsilon_{xx} = \frac{\partial u(x, z)}{\partial x} + \frac{1}{2}\left[\left(\frac{\partial u(x, z)}{\partial x}\right)^2 + \left(\frac{\partial w(x)}{\partial x}\right)^2\right] \tag{6}$$

provides a non-linear formulation for the strain-displacement relation. Following the small strains assumption, the first term in the squared brackets can be neglected, i.e. $(\partial u(x, z)/\partial x)^2 \approx 0$. The second term, $(\partial w(x)/\partial x)^2$, denotes the rotation of a line perpendicular to the beam axis, which for slender beams may be moderate or even large for small strains. From these assumptions and by inserting the kinematic relation given in Eq. 5, the final non-linear uniaxial strain-displacement relation

$$\varepsilon_{xx} = \underbrace{\frac{du(x)}{dx} - z\frac{d^2w(x)}{dx^2}}_{\varepsilon_{lin}} + \frac{1}{2}\left(\frac{dw(x)}{dx}\right)^2 \tag{7}$$

is obtained. The cut loads and the stress distribution are related by the requirement that all stresses shall be statically equivalent to all cut loads at any point on the beam. This results in the equivalence expression for the normal force

$$N(x) = \int_A dN = \int_A \sigma(x, z)dA \tag{8}$$

and for the bending moment

$$M(x) = \int_A z dN = \int_A z\sigma(x, z)dA \tag{9}$$

where A is the cross-sectional area. Inserting Hook's law from Eq. 2 and the non-linear strain formulation from Eq. 7 into Eqs. 8 and 9 results in the constitutive relations

$$\begin{aligned}
N(x) &= EA\left[\frac{du(x)}{dx} + \frac{1}{2}\left(\frac{dw(x)}{dx}\right)^2\right] \\
M(x) &= -EI_y\frac{d^2w(x)}{dx^2}.
\end{aligned} \tag{10}$$

Finally, the expressions for $N(x)$ and $M(x)$ are inserted into Eq. 4, which after reformulation yields the coupled non-linear partial differential equation

$$EI_y \frac{d^4 w(x)}{dx^4} - EA\left[\frac{du(x)}{dx} + \frac{1}{2}\left(\frac{dw(x)}{dx}\right)^2\right]\frac{d^2 w(x)}{dx^2} = q(x) - n(x)\frac{dw(x)}{dx} \tag{11}$$

to describe the geometric non-linear deformation of the beam.

A positive normal force N acting on the beam results in a tensile load, whereas a negative normal force results in a compressive load. Assuming a constant load per length $q(x) = q_0$ acts on the beam, in the non-linear case, the vertical deflection $w(x)$ will vary according to N

$$\begin{aligned} w(x) &< w_{lin}(x), \text{ if } N > 0, \\ w(x) &> w_{lin}(x), \text{ if } N < 0, \end{aligned} \tag{12}$$

with $w_{lin}(x)$ being the deflection for $N = 0$ (linear solution). This implies two important facts. Firstly, the stiffness K of the beam changes according to the magnitude and direction of the normal force acting on the beam. A tensile load increases K, which is why a guitar string has higher pitch for larger tension. Vice versa, a compressive load decreases K. Secondly, the bending moment M increases compared to the linear case if the beam is under compression. This can be shown by solving Eq. 11 numerically and means that a linear solution of a beam under compression is not conservative, thus potentially unsuitable for safe structural sizing.

In the case of non-linear FEM analysis, an iterative solution sequence, e.g. the Newton-Raphson method is required to solve the coupled non-linear problem in Eq. 11. Furthermore, the following features should be noted [18]:

- The principle of superposition does not hold.
- Analysis can be carried out for one load case at a time.
- The history (or sequence) of loading influences the response.
- The initial state of the system (e.g. pre-stress) may be important.

The tangent stiffness matrix of a converged non-linear FEM solution consists of a linear and a non-linear term

$$\mathbf{T} = \mathbf{K}_{lin} + \mathbf{K}_{nl} \tag{13}$$

which follow directly from the non-linear strain-displacement relation, e.g. the Green-Lagrange formulation given in Eq. 6. The non-linear term $\mathbf{K}_{nl}$ is sometimes referred to as differential stiffness. The interested reader may refer to the following books [18, 19] for further details on definition of the tangent stiffness matrix in non-linear FEM formulations.

3 PARAMETRIC STUDY

The Conceptual Load Analysis (CLA) tool was developed at the DLR in the framework of [5]. The tool estimates the wing and strut structural masses based on an aeroelastic conceptual approach considering empirical estimations as well as loads from 13 different load cases. A build-in solution sequence (*convergence*) sizes the structure of the wing and strut based on strength, buckling, and minimum thickness requirements. An optimization routine (*optimization*) iterates over the *convergence* routine including static aeroelastic effects to find the minimum structural mass of wing and strut for a given geometry. The output of the tool are MSC Nastran input cards modeling the structural components as so-called BAR elements with their estimated stiffness distributions based on the selected materials. A brief overview of the tool's methodology and the results of the parametric studies are presented in the following.

The wing planform is divided into four sections with rectangular wingboxes defined by the location of the Front Spar (FS) and Rear Spar (RS) provided as input. A straight Load Reference Axis (LRA) runs through the center of the wingboxes and defines the wing sweep Λ. The LRA is the reference axis for calculation of the wing internal loads and deflections.

The wing is discretized in ten bays for the calculation of aerodynamic forces and moments and eleven sections for the calculation of inertia forces and moments. The strut is modeled similar to the wing with a rectangular wingbox. A constant chord c_{st} is provided as input.

The aeroelastic module calculates the aeroelastic lift distribution and simulates two static aeroelastic effects, namely aeroelastic divergence and aileron efficiency. It consists of a swept beam structural model and Aerodynamic Influence Coefficients (AIC) for the aerodynamic model. The AICs are calculated by a simplified Vortex Lattice Method (VLM) with a single panel in chordwise direction. The structural model consists of three Structural Influence Coefficient (SIC) matrices relating the loads to the displacements at each section. Linear relationships connect the local lift loading and aerodynamic pitching moment at each bay to the local twist deformation. The additional stiffness provided by the strut is included by assuming equal deformations of wing and strut at the junction.

The aerodynamic module finds the zero-lift "jig" shape of the wing by dividing the lift distribution into two components, the lift distribution due to angle of attack and the zero-lift distribution. The zero-lift distribution is obtained by subtracting the desired lift distribution at the design cruise condition from the lift distribution due to angle of attack calculated by the aeroelastic module. The design lift-distribution is provided as input with the bell-shape factor $N_{bell} \in [1;6]$ and is shown in Fig. 4. It is calculated by the analytical expression

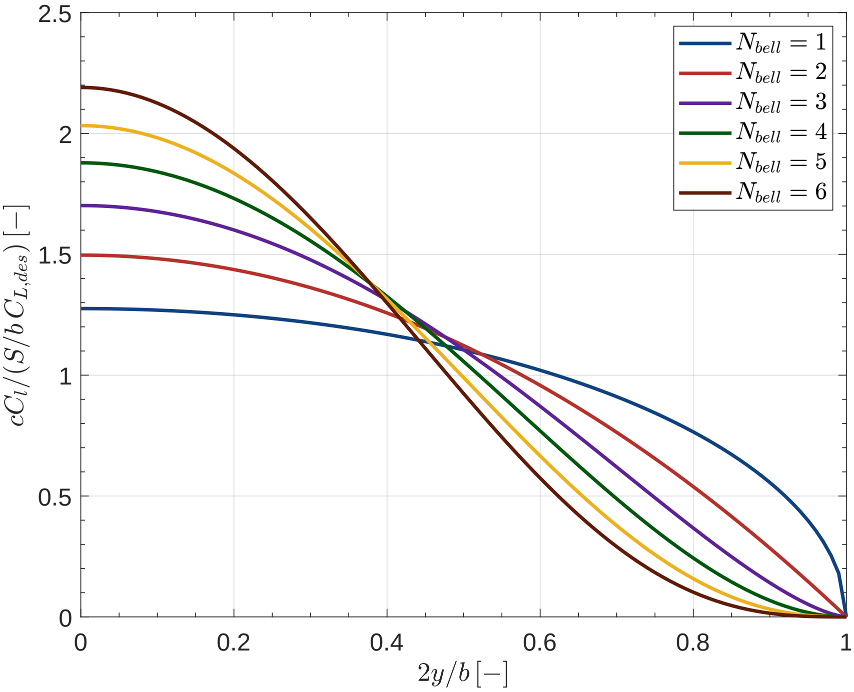

Figure 4: Non-dimensional design cruise lift distribution for six different bell-shape factors.

$$(cC_{l,des})_i = \frac{S}{b} C_{L,des} \frac{\sin^{N_{bell}}(\arccos(\eta_i))}{-0.0017 N_{bell}^3 + 0.0279 N_{bell}^2 - 0.1877\, N_{bell} + 0.9455} \tag{14}$$

where $(cC_{l,des})_i$ is the product of the local chord and the local lift coefficient of the ith bay, S is the reference wing area, b is the wing span, $C_{L,des}$ is the lift coefficient of the aircraft at the design cruise condition and η_i is the non-dimensional spanwise position of the ith bay. For $N_{bell} = 1$, the lift distribution is elliptical, whereas for larger values the lift is shifted inboard assuming a bell-like shape and reducing the bending moment at the wing root. The design cruise lift coefficient $C_{L,des}$ is calculated for a stationary horizontal flight by

$$C_{L,des} = \frac{mg}{\frac{1}{2}\rho V_{MO}^2}, \tag{15}$$

where ρ is the air density at the design cruise altitude H_{des} following the International Standard Atmosphere (ISA) model and V_{MO} is the maximum operating airspeed. The mass m is assumed from the Maximum Take-Off Mass (MTOM) and the Maximum Zero-Fuel Mass (MZFM) as

$$m = \frac{\text{MTOM} + \text{MZFM}}{2}. \tag{16}$$

The parameters H_{des} , V_{MO} , MTOM and MZFM are provided as inputs.

The 13 load cases are expected to be critical for sizing the wing and strut load-carrying structures and include: low- and high-speed maneuver cases for minimum and maximum values of the load factor n_z, positive and negative gust cases, roll cases, one landing case, one fatigue case at the design cruise condition, and one bump on ground case. All load cases assume only the MTOM condition, except for the maneuver load cases, which are repeated for the MZFM condition. The maneuver speed V_A for the low-speed maneuver case is calculated assuming a maximum lift coefficient $C_{L,max} = 1.3$. The cruise speed V_C is assumed equal to V_{MO}. The dive speed is approximated by $V_D = V_C +$ 25.6 ms^{-1}, where 25.6 ms^{-1} is the analytical solution of the simplified equation of motion $\dot{V} = g\,\sin(\gamma)$ solved for a 20 seconds dive at a path angle $\gamma = 7.5°$. The gust load cases are calculated for a constant Δn_z following two different certification specification procedures. All load cases, except for the fatigue load case, are considered to be limit loads with safety factors of 1.5 applied to the structure in sizing.

The global aircraft loads are distributed over the wing and integrated to obtain the internal shear force, bending moment, and torsion loads for each load case over the wing LRA. The distributed loadings are constant over each bay. Concentrated loads such as engines and landing gear reaction are also included. Since the wing section inboard of the strut constitutes a statically overdetermined system, finding the internal loads requires the bending stiffness distribution EI of the inboard wing to be known to apply additional deflection constraints. To avoid the inclusion of an iterative method, the CLA tool assumes a simplified strut reaction, where all wing sections inboard of the strut are subject to the same shear force, bending moment, and torsion moment as at the strut attachment.

The wing and strut load-carrying structure is represented by a box beam section. For the wing, it is assumed that the webs carry shear and torsion. The stringers carry only bending and the skins carry bending and torsion. The webs are sized for strength requirements, while the covers are also sized for fatigue and buckling requirements. For the strut, the load-carrying structure consists of covers and spars, which are sized for strength and buckling requirements. The material properties of the structural components are selected by the user from a pre-defined deck in the tool. The total structural mass of the SBW system is the sum of the load-carrying structural mass of the wing and strut as well as empirically estimated secondary mass contributions.

A parametric study with the CLA tool for the AWATAR configuration has been performed in [14] to find optimal configurations with minimum structural mass of the wing and strut. The parametric variation includes the strut attachment position on the wing span η_{st} and chord ξ_{st}, the strut sweep angle, the chordwise engine position, and the design cruise lift distribution shape factor. The results, summarized in Tab. 1, are briefly discussed in the following.

Table 1: Comparison of the AWATAR configurations modeled in the CLA tool

Configuration	$\boldsymbol{\eta_{st}}$ **[-]**	$\boldsymbol{\xi_{st}}$ **[-]**	$\mathbf{m_w}$ **[kg]**	$\mathbf{m_{st}}$ **[kg]**	$\mathbf{m_{SBW}}$ **[kg]**
Baseline	0.5	0.19	9836	4485	14321
Baseline-AE	0.5	0.19	21561	5718	27279
C1	0.45	0.18 (FS)	10620	2434	13054
C1-AE	0.45	0.18 (FS)	20736	2486	24222
C2	0.45	0.63 (RS)	13004	5476	18480

Three optimized configurations result from two parametric studies. The first parametric optimization routine does not take aeroelastic constraints into consideration, i.e. only the *convergence* solution sequence is executed. This means that the load carrying structure is sized only for the internal loads resulting from the 13 load cases, while static aeroelastic effects (divergence and aileron effectiveness) are neglected. The resulting optimal configuration, denoted as "C1", has a total mass of 13054 kg. However, this configuration is subject to aileron reversal at 1.15 V_D according to the CLA tool. The *optimize* solution sequence can be executed to achieve a feasible aeroelastic design of C1. The resulting adapted configuration C1-AE ("Aileron Effectiveness") shows a drastic increase of 86% in structural mass of the SBW. This results from the additional torsional stiffness required in the wing to provide adequate aileron effectiveness. To achieve this, the optimizer radically increases the thickness of the wingbox by a factor of five in the region of the strut attachment. A similar result was found in the design of a SBW configuration with the CLA tool in [20], where the SBW structural mass increase caused by the inclusion of the aileron effectiveness constraint was 76%.

Considering the radical increase in structural mass associated with the aileron effectiveness requirement, a second parametric optimization routine, which includes the aeroelastic constraints, i.e. executes the *optization* solution sequence, is performed in order to find an optimal and aeroelastic feasible configuration of the AWATAR aircraft. The resulting configuration, denoted as "C2", is 42% heavier than C1, but 24% lighter than C1-AE. The inclusion of the aeroelastic constraints in the optimization routine shifts the optimal chordwise strut attachment position from the FS (C1 and C1-AE) to the RS (C2). This is because a strut attached at the RS acts against the pitch down behavior of an aileron deflected downward, thus supporting its effectiveness.

The optimal spanwise strut attachment position is chosen at 45% the semi-span for all three configurations. This ensures comparability between the configurations and relates closely to the baseline configuration provided by Onera, where $\eta_{st} = 0.5$, as well as to the SUGAR high speed configuration, where $\eta_{st} = 0.57$ [21]. All configurations are modeled with a quasi-elliptical design cruise lift distribution ($N_{bell} = 2$). Note that the baseline configuration breaks the aileron effectiveness constraint if only the *convergence* solution sequence is executed. Hence, a second,

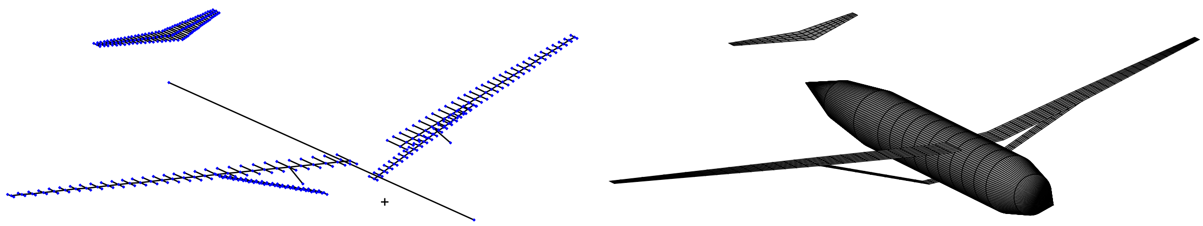

Figure 5: Beam model and aerodynamic panel model for configuration C1.

aeroelastic feasible baseline "AE" configuration stiffened by the *optimization* solution sequence is included in Tab. 1

The exported beam model and aerodynamic panel model are shown for configuration C1 in Fig. 5. The wing, strut, and Horizontal Tail Plane (HTP) include massless nodes along the Leading Edge (LE) and Trailing Edge (TE) for visualization purposes. The fuselage is modeled as a slender body, while the other lifting surfaces are modeled by panels. The ailerons are defined at the non-dimensional spanwise positions $\eta_{\delta_a,in} = 0.70$ and $\eta_{\delta_a,out} = 0.88$ with a chord of 25% the local wing chord. They are defined as aerodynamic control surfaces. Similarly, the HTP is defined as an aerodynamic control surface to be used as a trim variable during the aeroelastic trim analysis. The hinge line is defined perpendicular to the x axis at 40% of the HTP root chord.

Braced wing configurations usually include a curved wing-strut junction, as shown for the baseline AWATAR configuration in Fig. 2. This mitigates the strong aerodynamic interference effects in that region, which have been found in previous works [21, 22]. The exported beam models from the CLA tool do not include a refined junction. The straight strut intersects the wing with the angle Φ. A simple modeling approach for the wing-strut junction is adapted here by including a vertical beam element between the wing and the strut tip to create a vertical offset. The junction, referred to as "elbow", is illustrated in Fig. 6. The length of the vertical element z_{st} is defined relative to the strut length l_{st}, as shown in Fig. 6a. Fig. 6b shows the additional aerodynamic panels for the elbow element.

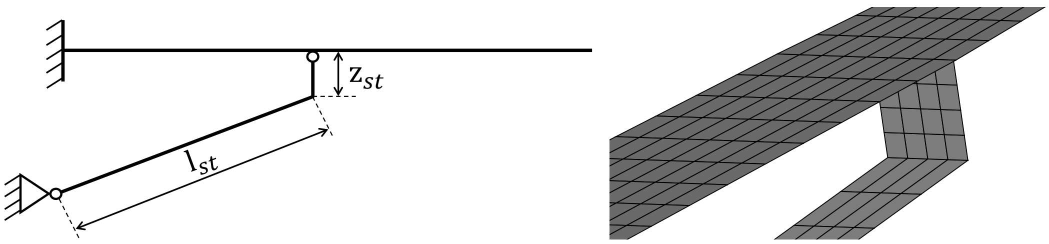

(a) Illustration of the elbow element. (b) Aerodynamic panels on the elbow element.

Figure 6: Illustration of the elbow element and its aerodynamic panels.

4 AEROELASTIC ANALYSIS

Two maneuver load cases are considered for the aeroelastic analysis presented in this section, namely a pull-up maneuver at the dive speed V_D with a load factor $n_z = 2.5\,g$ (denoted as "VD+") and a push-down maneuver at the cruise speed V_C with $n_z = -1\,g$ (denoted as "VC-). First, the linear aeroelastic trim analysis is performed in MSC Nastran with SOL144 to find the internal and external loads acting on the aircraft. Additionally, the aileron effectiveness is calculated for flight speeds spanning the AWATAR flight envelope to validate the results obtained with the CLA tool. The nodal forces resulting from the trim analysis are applied in static linear (SOL101) and non-linear (SOL106) analyses to assess the effects of geometric non-linearity on the internal load distribution in the wing and strut. Finally, the pre-stressed flutter analysis is conducted by including the tangent stiffness matrix of a converged non-linear static solution in the general flutter equation. The methodology is depicted in Fig. 7.

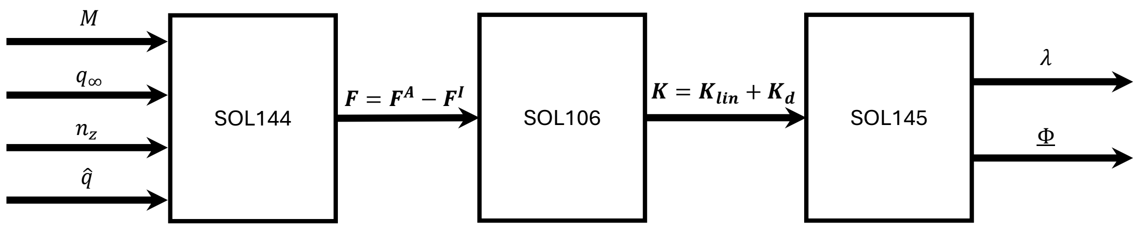

Figure 7: Pre-stressed flutter analysis workflow.

4.1 Trim analysis

The load cases are defined following the speed definitions of the CLA tool discussed in Sect. 3 and are normalized at sea level. The trim variables include the aircraft angle of attack and the incidence angle of the HTP. The trim analysis is performed with the aeroelastic solver SOL144. As for all aeroelastic solvers in MSC Nastran, a linear structural model is assumed. The AIC matrices are calculated following the internal DLM method without the inclusion of correction factors. An incompressible flow is assumed throughout the aeroelastic analysis in this section, unless otherwise stated. This ensures that non-linear effects are separated from effects arising due to compressibility.

The inputs for the trim analysis include the Mach number ($M = 0$ for incompressible flow), the dynamic pressure q_∞, the load factor n_z, and the non-dimensional pitch rate $\hat{q}$ to simulate the quasi-steady maneuver. The output of the trim analysis includes the trim values of the trim variables α_{trim} and i_{trim}, the structural deformations, the internal load and stress distributions, and the aerodynamic and inertia forces. The difference between the aerodynamic forces $\mathbf{F}_A$ and inertia forces $\mathbf{F}_I$ is saved in matrix form to be applied in subsequent static analyses

$$\mathbf{F} = \mathbf{F_A} - \mathbf{F_I} \tag{17}$$

where $\mathbf{F}$ is referred to as ”combined forces”. The combined forces can be applied at the structural nodes to perform linear and non-linear static simulations, as presented in the following.

4.2 Static analysis

The effects of the geometric non-linear formulation derived in Sect. 2 on the deformations and internal loads of the structure can be compared to the linear results from the trim analysis. It is important to note that the boundary conditions of the model change between the trim analysis and the static analysis, since no inertia relief is included in this work. In the trim analysis, the model is free to plunge in z direction and to pitch around the y axis. In the static analysis, all DOFs are constrained by clamping the model at the fuselage center node. However, it will be shown in the following that the change in model constraints between the trim analysis and the linear static analysis does not alter the results significantly.

Fig. 8 shows the bending moment at the strut LRA $M_{x,st,LRA}$ and the normal force in the strut N_{st} for the VD+ and VC- load cases. The results are shown only for configuration C2, because the same qualitative trends arise for configurations C1 and C1-AE. In general, it can be observed that the solutions resulting from the trim analysis (blue curve) and the linear static

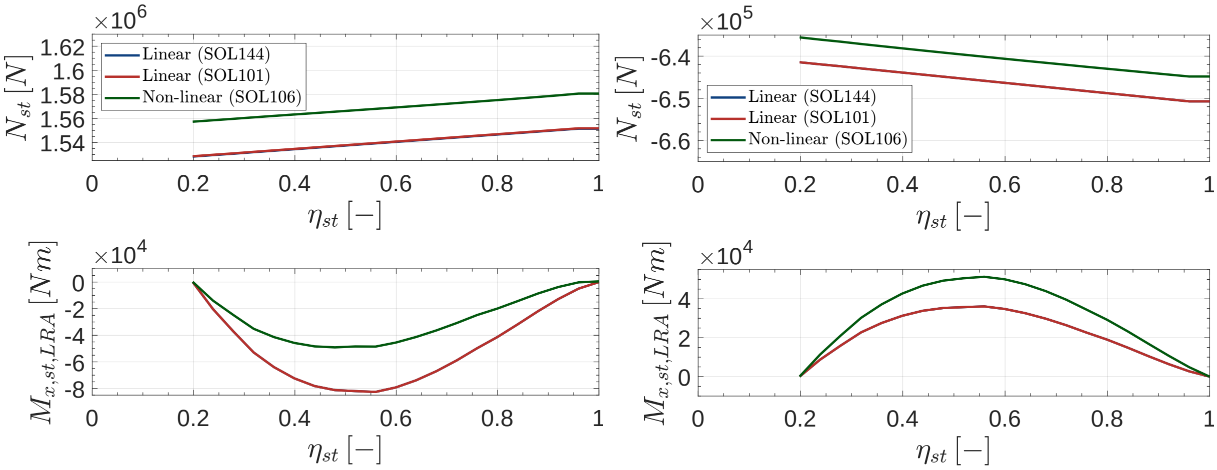

(a) VD+ load case.

(b) VC- load case.

Figure 8: Bending moment at the strut LRA and normal force for the VD+ and VC- load cases; configuration C2.

analysis (crimson curve) are very similar, which is a desired result, since it confirms the comparability between the two solution sequences. In fact, the blue curve is barely visible, because the results are almost identical. The bending moment shown in Fig. 8a for the pull-up maneuver is significantly larger for the linear solution sequences compared to the non-linear one (green curve). This is an expected result following the discussion on Eq. 12 for the geometric non-linear deformation of a beam element. The upward wing bending induces a tensile load in the strut, which results in a stiffening effect. Vice versa, for the push-down maneuver shown in Fig. 8b, the bending moment in the strut is significantly larger for the non-linear solution than for the linear ones since the strut is subject to a compressive load.

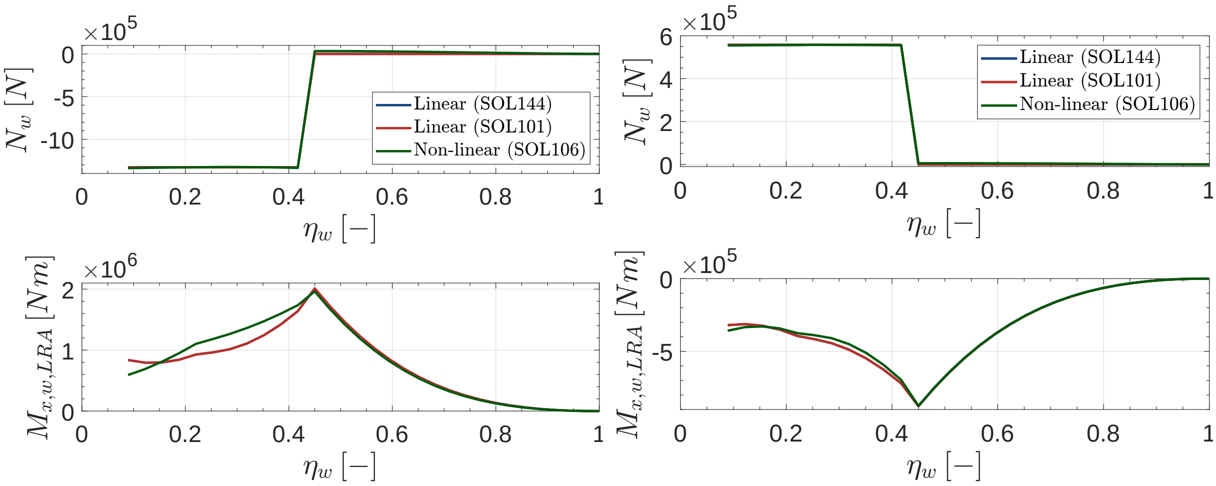

(a) VD+ load case.

(b) VC- load case.

Figure 9: Bending moment at the wing LRA and normal force for the VD+ and VC- load cases; configuration C2.

Fig. 9 repeats the same analysis for the wing. For the pull-up maneuver, the normal force in the inboard section of the wing N_w is negative, as shown in Fig. 9a. Thus, the inboard section of the wing is subject to a compressive load. The non-linear effect on the wing bending moment is clearly visible in the diagram below, where larger values of $M_{x,w,LRA}$ result for most part of the inboard wing for the geometric non-linear formulation compared to the linear ones. Again, the opposite result is found for the push-down maneuver shown in Fig. 9b, where the linear formulations provide conservative results since the inboard wing is subject to a tensile load. Note that the normal force in the inboard section of the wing results directly from the

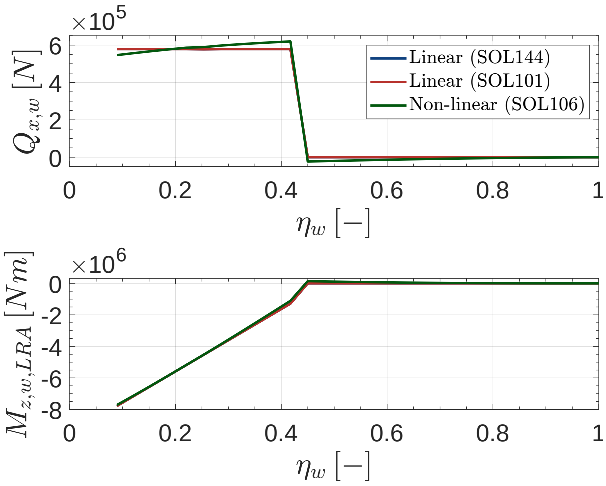

(a) VD+ load case.

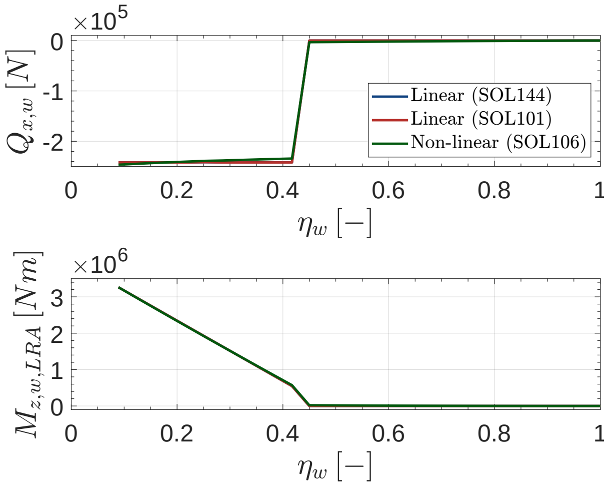

(b) VC- load case.

Figure 10: Wing in-plane shear force and bending moment for the VA+ and VA- load cases; configuration C2

strut reaction force and has the opposite sign, hence $\text{sign}(N_w) = -\text{sign}(N_{st})$. The magnitude of N_w depends on the difference in sweep between the wing and the strut with the maximum resulting for equal sweep angles. Therefore, for any given load case, either the inboard wing or the strut will be subject to a compressive load, for which the geometric non-linear formulation will provide conservative results compared to the classical linear analysis.

If the difference in sweep between the wing and strut is not equal to zero, the magnitude of N_w reduces and an in-plane shear force $Q_{x,w}$ and bending moment $M_{z,w,LRA}$ develop in the wing. The in-plane loads resulting from the two load cases VD+ and VC- are shown in Fig. 10 for configuration C2. The tensile force in the strut resulting from the pull-up maneuver induces a positive in-plane shear force in the inboard section of the wing, as shown in Fig. 10a. The non-linear solutions produce larger values up until $\eta_w \approx 0.2$. The absolute value of the in-plane bending moment increases linearly inboard of the strut, reaching a maximum value of approximately $-7.7 \cdot 10^6$ Nm.

Fig. 10b shows the in-plane loads for the push-down maneuver. The in-plane shear force shows again a step response at the strut attachment, "jumping" from zero to approximately $-2.2 \cdot 10^5$ N. The in-plane bending moment increases linearly from the strut attachment to the wing root reaching a maximum value of approximately $3.1 \cdot 10^6$ Nm.

The CLA tool does not calculate the in-plane loads and neglects them in the sizing of the structure. However, Fig. 10 shows that the in-plane loads for the SBW configuration can be four times larger than the out-of plane loads. The in-plane bending moment may potentially overload the wingbox structure near the wing root. This effect can be mitigated by integrating a backwards swept strut to reduce the difference in sweep between the wing and the strut. This would increase the axial loading in the inboard wing, requiring a detailed structural sizing routine that includes in-plane loads to determine the optimal mass configuration.

4.3 Aileron effectiveness

Reduced aileron effectiveness inside the flight envelope is a common challenge for braced wing configurations due to the slender and elongated wing with relatively low torsional stiffness. Aileron reversal has been found in previous research programs including the SUGAR configuration [20, 23], as well as in this work for the AWATAR configurations modeled in the CLA tool.

The local increase in lift from an aileron deflection causes a torsional moment, which produces a twist deformation of the flexible wing and reduces the local AoA. Therefore, the additional lift due to an aileron deflection may be positive, zero, or negative. The aileron effectiveness is defined by the ratio of the aileron control derivative for the elastic wing to the aileron control derivative for the rigid wing $C^{elastic}_{l,\delta_a}/C^{rigid}_{l,\delta_a}$. At low dynamic pressures, the aileron effectiveness is close to one. Increasing the airspeed may decrease the aileron effectiveness, especially for ailerons placed far outboard of HARW configurations.

SOL144 provides the control derivatives for aerodynamic control surfaces. The ailerons are defined for all three configurations according to the definitions for $\eta_{\delta_a,in}$ and $\eta_{\delta_a,out}$ provided in Sect. 3. Fig. 11 shows the results for the aileron effectiveness of the baseline configurations. The unsplined rigid control derivative and the unrestrained elastic control derivative are shown. The red dashed line indicates the aeroelastic requirement of minimum 10% aileron effectiveness up until $1.15V_D$, as defined in the CLA tool. Fig. 11a includes the effect of compressibility (cross markers). The results show very good agreement with the results obtained with the CLA tool. Configuration C1 infringes the requirement well inside the flight envelope at around 174 ms^{-1} in the incompressible case and already at 166 ms^{-1} if compressibility effects are included. Both configurations C1-AE and C2 provide adequate aileron effectiveness for the required speed range in the incompressible case. However, only C1-AE fulfills the requirement if compressibility effects are included. Fig. 11b shows the effect of a 4% elbow (dotted lines), which generally degrades the aileron performance compared to the baseline configurations. Configuration C1-AE$_{4\%}$ is the only elbow configuration that fulfills the aeroelastic requirement.

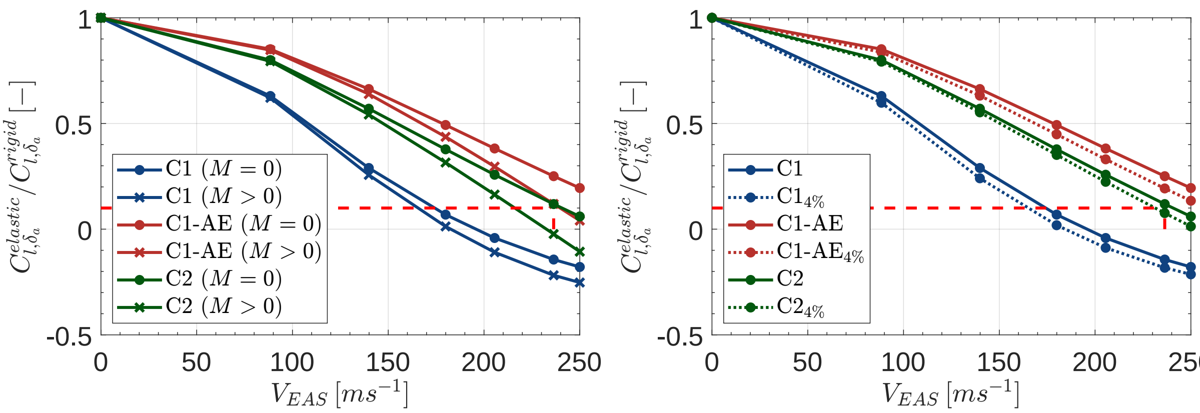

(a) Effect of compressibility.

(b) Effect of elbow.

Figure 11: Aileron effectiveness for the baseline configurations C1, C1-AE, and C2 including the effects of compressibility and of the 4% elbow element

4.4 Flutter

Aeroelastic flutter is the dynamic instability of an elastic body in an airstream. It is an unstable, self-excited vibration in which the structure extracts energy from the airstream, and often results in catastrophic structural failure. Below the flutter speed, the oscillations are damped. Above the flutter speed, one mode becomes positively (or negatively, depending on the definition) damped, resulting in unstable oscillations.

The flutter analysis is performed with SOL145 in MSC Nastran for the restrained configurations

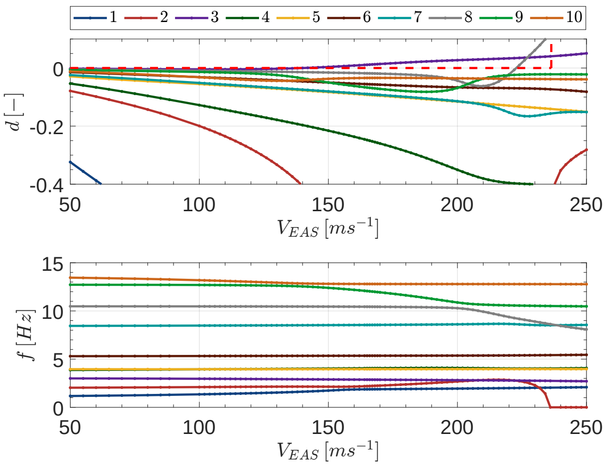

(a) Incompressible.

(b) Compressible.

Figure 12: V-d and V-f diagrams for the first ten flexible modes resulting for the restrained configuration C2 including compressibility effects.

C1-AE and C2 using the *pk*-method. The analysis is performed at sea level. The restrained models consist of the right wing and strut only, since the fixed condition at the fuselage center node effectively decouples the left and right side of the symmetry plane. The fully clamped condition allows for the application of the combined loads from the load cases VD+ and VC- on the structure with SOL106. The differential stiffness resulting from the converged non-linear static solution can then be included in the flutter analysis, as illustrated in Fig. 7. The results of the flutter analysis for the restrained models without pre-load are presented first, including compressibility effects and the effect of a 4% elbow element. Finally, a discussion on the effect of non-linear prestress on the flutter mechanism concludes this chapter.

Fig. 12 shows the V-d and V-f diagrams for configuration C2. Only the first ten modes are considered, because it was found that the higher frequency modes are not critical for the flutter cases discussed here. The V-d diagram shown on the top includes a dashed red line, which indicates the flutter boundary ($d = 0$) up until $1.15V_D$. For the incompressible case shown in Fig. 12a, mode 3 becomes unstable at $V_f = 140$ ms^{-1}. Mode 3 corresponds to the first wing torsion. It shows a soft flutter behavior, because it crosses the flutter boundary at a shallow angle. The flutter speed is only 9% larger than the design cruise speed normalized at sea level and well within the flight envelope, indicating that configuration C2 does not provide adequate flutter stability. A hard flutter case appears for mode 8 at 223 ms^{-1}. Mode 8 is characterized by the second in-plane wing bending. The V-f diagram shows that the frequencies of modes 8 and 9 approach each other at around 200 ms^{-1} and then diverge, which could indicate mode switching or coalescence.

The effects arising from compressibility on the flutter results are shown in Fig. 12b. The flutter speed is significantly increased to $V_f = 222$ ms^{-1}. The flutter boundary is crossed at a steep angle by mode 10, which is characterized by the second wing torsion. The frequency of mode 10 decreases sharply to approximately 7.1 Hz just before the mode becomes unstable. Mode switching for modes 3 and 4 at around 200 ms^{-1} can be observed in the V-d diagram by the singularity in the violet and green curves. Mode 4 crosses the flutter boundary at a shallow angle at 224 ms^{-1}.

It should be noted that the increased flutter speed of configuration C2 resulting from the inclusion of compressibility effects is not valid for the configurations with the strut attached at the

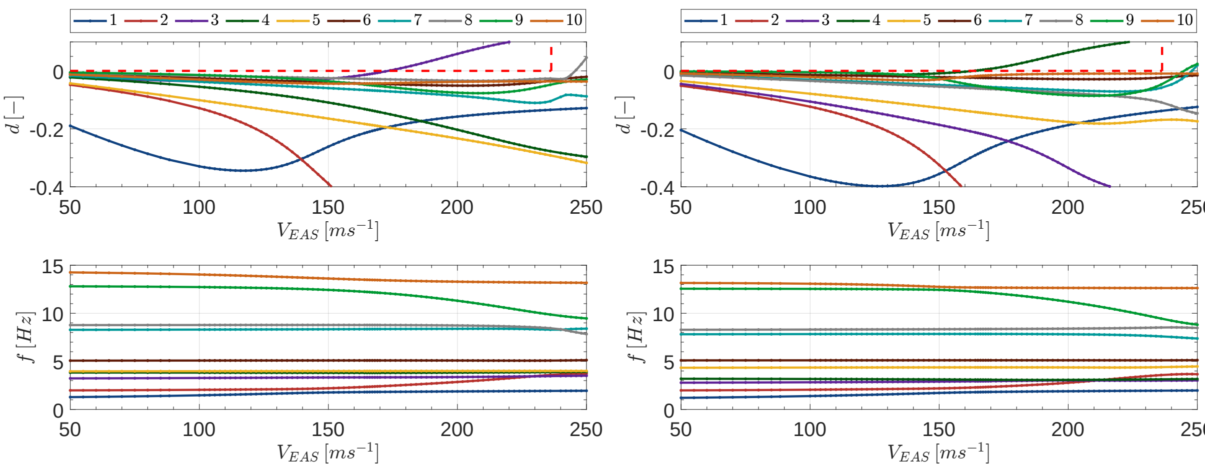

(a) C1-AE. (b) C1-AE with a 4% elbow element.

Figure 13: V-d and V-f diagrams for the first ten flexible modes resulting for the restrained configuration C1-AE with and without a 4% elbow element.

FS. In the case of configurations C1 and C1-AE, the flutter speed is actually decreased by 2% and 9% respectively, if compressibility effects are included.

Fig. 13 shows the flutter results for the restrained configuration C1-AE. For the baseline configuration, the flutter boundary is crossed by mode 3 at $V_f = 173\ \mathrm{ms}^{-1}$, as shown in Fig. 13a. This mode is characterized by the second wing bending coupled with the first wing torsion. The V-f diagram shows that modes 2, 3, 4, and 5 have closely spaced frequencies, however, no visible coalescence can be identified in the diagram.

The inclusion of the 4% elbow element slightly degrades the flutter results, as shown in Fig. 13b. The flutter speed is reduced to $V_f = 165\ \mathrm{ms}^{-1}$, where mode 4 crosses the flutter boundary at a shallow angle, producing a soft flutter case. It is important to mention, that mode 4 of the elbow configuration is also characterized by the second wing bending with the first wing torsion, but the torsional motion is significantly larger in magnitude than for the baseline configuration. Additionally, the first strut bending also appears in this mode.

Non-linear pre-stress is included in the flutter analysis by replacing the linear stiffness matrix **K** in the general flutter equation for an undamped system [24]

$$\left[\frac{V^2}{c^2}\mathbf{M}p^2 + \mathbf{K} - q_\infty \mathbf{Q}\right]\underline{d} = \underline{0}. \tag{18}$$

by the tangent stiffness matrix **T** of a converged non-linear static solution. It is important to note that the pre-stressed condition from the load case does not, in general, correspond to the actual pre-stressed condition at the flutter speed, since the flutter speed is usually not equal to the speed of the load case. Furthermore, the structural deformations resulting from the load case are not considered in the pre-stressed flutter analysis. The intention of the direct approach implemented in this work is to understand if and to what extend non-linear pre-stress influences the aeroelastic characteristics of the SBW configuration.

Fig. 14 shows the flutter results for configuration C2 considering geometric non-linear pre-stress from the VD+ and VC- load cases. For the VD+ load case shown in Fig. 14a, the system is stabilized by the pre-stressed condition and is flutter free within the $1.15V_D$ boundary. However, for the VC- load case shown in Fig. 14b, the torsional mode 3 of the wing becomes unstable at

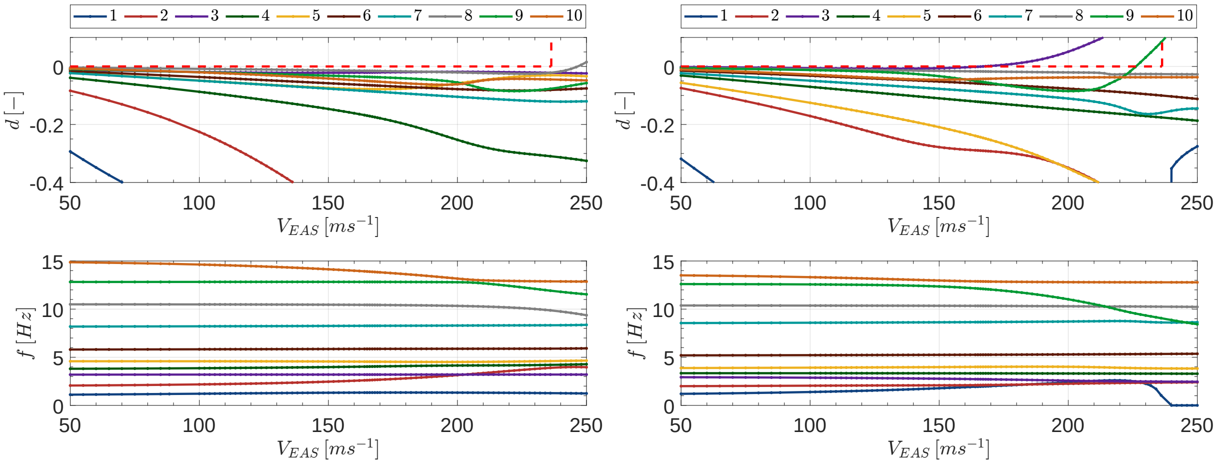

(a) VD+ load case. (b) VC- load case.

Figure 14: V-d and V-f diagrams for the first ten flexible modes resulting for the restrained configuration C2 considering geometric non-linear pre-stress from the VD+ and VC- load cases.

$V_f = 167\ \text{ms}^{-1}$. While this flutter speed is 27 ms^{-1} larger than for the unloaded configuration C2, it is still well within the flight envelope of the AWATAR aircraft. Hard flutter occurs for the highly coupled mode 9 at 226 ms^{-1}. A correlation analysis has been performed by computing the Modal Assurance Criterion (MAC) matrix for the normal modes of the unloaded and pre-stressed model. Configuration C2 provides good correlation values along the matrix diagonal, indicating that the normal mode shapes of the pre-stressed model and the unloaded model are similar. The flutter mechanism, described by the complex eigenvector of the critical mode at the flutter speed, does not change significantly with the inclusion of non-linear prestress. The first strut bending appears for the VC- load case due to its reduced stiffness caused by the compressive load. This affects also the flutter frequency, which decreases from 2.90 Hz in the unloaded case to 2.71 Hz.

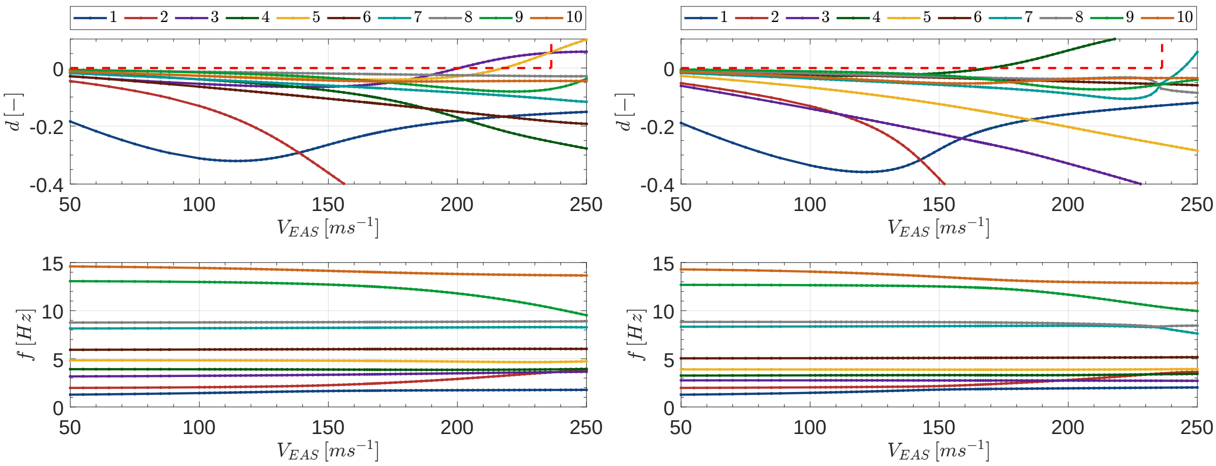

(a) VD+ load case. (b) VC- load case.

Figure 15: V-d and V-f diagrams for the first ten flexible modes resulting for the restrained configuration C1-AE considering geometric non-linear pre-stress from the VD+ and VC- load cases.

The same analysis is presented for configuration C1-AE in Fig. 15. For the VD+ load case shown in Fig. 15a, soft flutter appears for mode 3 at $V_f = 200\ \text{ms}^{-1}$. This flutter speed is 16% larger than for the unloaded configuration C1-AE. The resulting flutter mechanism is again similar to that of the unloaded case. The flutter frequency increases from 3.33 Hz in the unloaded case to 3.49 Hz. At 218 ms^{-1}, mode 5 crosses the flutter boundary. This critical mode was not found for the unloaded configuration. The resulting flutter mechanism includes in- and out-of-plane bending of the outboard wing section and does not correlate to the normal modes of the modal base. The flutter frequency is 4.67 Hz.

For the VC- load case, the flutter boundary is crossed at $V_f = 170\ \mathrm{ms}^{-1}$ by mode 4 at a shallow angle, as shown in Fig. 15b. The computation of the MAC matrix indicates that mode 4 of the pre-stressed model correlates with mode 3 of the unloaded model. Therefore, the critical mode of the pre-stressed model actually corresponds to the critical mode of the unloaded model for the VC- load case. The resulting flutter mechanism at 3.30 Hz is similar to that described above with the noticeable inclusion of the first strut bending. This results from the compressive load in the strut, which reduces its stiffness.

5 CONCLUSION AND OUTLOOK

The SBW configuration allows for the implementation of large AR configurations, which reduce the induced drag and improve in-flight efficiency. Three optimized configurations with minimum structural mass have been presented using a physics-based, semi-empirical CLA tool. The inclusion of the aileron effectiveness as an aeroelastic constraint leads to an increased structural mass and shifts the optimal strut attachment position from the FS to the RS. The inboard section of the SBW configuration constitutes an over-determined system with large axial loads in both the wing and the strut as well as large deformations due to the slender HARW. Therefore, the effects following from geometric non-linearity on the internal loads of the structural components and the dynamic aeroelastic response have been investigated in this work.

The static analysis shows that both the linear and non-linear formulations may yield conservative results for the internal loads of a structural component depending on the axial loading resulting from the load case. A conservative result for the strut bending moment is provided by a linear formulation, if a pull-up maneuver is considered. The non-linear formulation yields a conservative result for a push-down maneuver, because the strut is under compression. For the strut normal force, the opposite result is found. For a pull-up maneuver, the non-linear formulation yields a conservative result, whereas for a push-down maneuver, the linear formulation provides conservatism.

The wing normal force has the opposite sign of the strut normal force. Hence, conservative results for the wing bending moment are provided by the non-linear formulation for pull-up maneuvers and by the linear formulation for push-down maneuvers.

Finally, the static analysis shows that the inboard section of the wing is subject to significant in-plane loads. The in-plane bending moment at the wing root is approximately four times larger than the maximum out-of-plane bending moment and may overload the load-carrying structure, which is sized only for the out-of-plane shear force and bending moment by the CLA tool. A new structural sizing iteration considering the in-plane loads as well as the wing normal force is required to find new optimized configurations. A backwards swept strut is expected to reduce the in-plane loads.

The predictions made by the CLA tool on the aileron effectiveness have been validated with MSC Nastran. Configuration C1 shows aileron reversal around the design cruise speed, whereas configurations C1-AE and C2 fulfill the minimum aileron effectiveness requirement of 10% at $1.15V_D$ at sea level.

The flutter analysis has shown flutter instability within the flight envelope for both configurations C1-AE and C2. No clear coalescence of the critical eigenmodes could be identified around the flutter speed, however, the V-f diagrams show very closely spaced eigenmode frequencies. The flutter speed increases if non-linear pre-stress from the VD+ and VC- load cases is included in the flutter equation. A new critical mode may appear, as was the case for configuration C1-AE for the VD+ load case. The flutter mechanism of the pre-stressed configurations is, in general, very similar to that of the unloaded configurations. The first strut bending appears in the flutter mechanism for the push-down maneuver. The flutter frequency increases or decreases slightly for the pull-up or push-down maneuver respectively compared to the unloaded case.

The results obtained in this work are based on low fidelity beam models consisting of approximately 150 elements coupled with a linear aerodynamic model. The direct non-linear flutter analysis proposed in this work gives insight into the effects of geometric non-linearity on the flutter dynamics, but, in general, it is not representative of the actual flutter condition, since the differential stiffness arising from the non-linear pre-stress is calculated at the flight speed defined by the load case rather then at the actual flutter speed. Additionally, the DLM mesh does not deform with the structure. Therefore, the development and coupling of a high fidelity structural model with a deformable linear aerodynamic model is necessary to compare and validate the results obtained in this work, since the large deformations of the wing are expected to alter the aerodynamics significantly. An iterative solution method, where the pre-stress is calculated at the flutter speed may be more representative of the actual flutter dynamics of the system. Additionally, the inclusion of a non-linear aerodynamic model may give insight into non-linear aerodynamic effects, such as the transonic dip, which has been found for the SUGAR configuration during wind tunnel testing and which cannot be captured by the DLM method.

The development of an optimized high fidelity structural model would also allow for the comparison of the estimated mass and stiffness distributions of the wing and strut derived for the optimized configurations C1, C1-AE, and C2. Furthermore, the high fidelity model would allow for a detailed structural sizing of the pinned joints at both strut ends. These primary connection elements are expected to transmit large loads and must be designed according to safety critical design requirements.

Funding Statement: The work presented herein was performed in the project AWATAR and has been funded by the European Community's Horizon Europe Framework Programme under the Grant agreement ID 101140588.

6 REFERENCES

[1] European Union (2024). AWATAR (Advanced Wing Maturation and Integration). https://www.clean-aviation.eu/research-and-innovation/clean-aviation/clean-aviation-projects/awatar. Last accessed: 03 October 2025.

[2] Eisenhut, D., Moebs, N., Windels, E., et al. (2021). Aircraft requirements for sustainable regional aviation. *Aerospace*, 8(3). ISSN 2226-4310. https://doi.org/10.3390/aerospace8030061.

[3] International Air Transport Association (2026). IATA long-term air transport passenger demand projections.

[4] Ma, Y. and Elham, A. (2024). Designing high aspect ratio wings: A review of concepts and approaches. *Progress in Aerospace Sciences*, 145, 100983. ISSN 0376-0421. https://doi.org/10.1016/j.paerosci.2024.100983.

[5] Chizzotto, P. (2019). *Improving Aircraft Conceptual Design with Methods for Wing Loads, Aeroelasticity and Mass Estimation*. Ph.D. thesis, Technische Universität Berlin.

[6] Rothert, H. and Gensichen, V. (1987). *Nichtlineare Stabstatik, Baustatische Methoden Gundlagen und Anwendungen*. Berlin: Springer-Verlag.

[7] Dowell, E., Edwards, J., and Strganac, T. (2003). Nonlinear aeroelasticity. *Journal of Aircraft*, 40(5), 857–874. https://doi.org/10.2514/2.6876.

[8] Livne, E. (2001). Aeroelasticity of joined-wing airplane configurations: Past work and future challenges - a survey. https://doi.org/10.2514/6.2001-1370.

[9] Allen, T., Sexton, B., and Scott, M. J. (2015). *SUGAR Truss Braced Wing Full Scale Aeroelastic Analysis and Dynamically Scaled Wind Tunnel Model Development*. https://doi.org/10.2514/6.2015-1171.

[10] Coggin, J., Kapania, R., Zhao, W., et al. (2014). Nonlinear aeroelastic analysis of a truss based wing aircraft. *55th AIAA/ASMe/ASCE/AHS/SC Structures, Structural Dynamics, and Materials Conference*. https://doi.org/10.2514/6.2014-0335.

[11] Nguyen, N. T., Ting, E., and Lebofsky, S. (2015). *Aeroelasticity of Axially Loaded Aerodynamic Structures for Truss-Braced Wing Aircraft*. https://doi.org/10.2514/6.2015-1840.

[12] Sohst, M., d. V., J. L., Afonso, F., et al. (2022). Optimization and comparison of strut-braced and high aspect ratio wing aircraft configurations including flutter analysis with geometric non-linearities. *Aerospace Science and Technology*, 124, 107531. ISSN 1270-9638. https://doi.org/10.1016/j.ast.2022.107531.

[13] European Union (2024). Clean Aviation. https://www.clean-aviation.eu/. Last accessed: 03 October 2025.

[14] Colombo-Acquarone, D. (2026). *Investigation of Nonlinear Structural Dynamics and Aeroelastic Properties of Strut-braced Wings at a Conceptual Design Stage*. DLR-IB-AE-GO-2026-33, Technische Universität Berlin. https://elib.dlr.de/224239/.

[15] Hodges, D. and Pierce, G. (2002). *Introduction to Structural Dynamics and Aeroelasticity*. New York: Cambridge University Press.

[16] Krätzig, W., Harte, R., Meskouris, K., et al. (2005). *Tragwerke 2*. Berlin: Springer-Verlag.

[17] Reddy, J. (1993). *An Introduction to the Finite Element Method*. New York: McGraw-Hill.

[18] Reddy, J. (2015). *An Introduction to Nonlinear Finite Element Analysis*. Oxford: Oxford University Press.

[19] Bathe, K. (1996). *Upper Saddle River*. Oxford: Prentice Hall.

[20] Moerland, E., Pfeiffer, T., Böhnke, D., et al. (2017). *On the Design of a Strut-Braced Wing Configuration in a Collaborative Design Environment*. https://doi.org/10.2514/6.2017-4397.

[21] Harrison, N., Hoffman, K., Lazzara, D., et al. (2023). Subsonic ultra green aircraft research: Phase iv - final report - volume i - mach 0.80 transonic truss-braced wing high-speed design report. Tech. Rep. CR–20220016017 Volume I, NASA ; The Boeing Company.

[22] Ko, A., Mason, W., and Grossman, B. (2003). *Transonic Aerodynamics of a Wing/Pylon/Strut Juncture*. https://doi.org/10.2514/6.2003-4062.

[23] Bradley, M., Droney, C., and Allen, T. (2015). Subsonic ultra green aircraft research: Phase ii - volume i - truss braced wing design exploration. Tech. Rep. CR-2015-218704/Volume I, NASA ; The Boeing Company.

[24] Schwochow, J. (2012). *The Aeroelastic Stability Analysis - a practival Interval Approach of Uncertainty Aspects*. Ph.D. thesis, Universität Kassel.

COPYRIGHT STATEMENT